ADVANCED SCIENCE
Open Access
www.advancedscience.com

Check for updates

Light-Intensity Switching of Graphene/WSe_2 Synaptic Devices

*Hongyu Tang, Tarique Anwar, Min Seok Jang, and Giulia Tagliabue**

2D van der Waals heterojunctions (vdWH) have emerged as an attractive platform for the realization of optoelectronic synaptic devices, which are critical for energy-efficient computing systems. Photogating induced by charge traps at the interfaces indeed results in ultrahigh responsivity and tunable photoconductance. Yet, optical potentiation and depression remain mostly modulated by gate bias, requiring relatively high energy inputs. Thus, advanced all-optical synapse switching strategies are still needed. In this work, a reversible switching between positive photoconductivity (PPC) and negative photoconductivity (NPC) is achieved in graphene/WSe_2 vdWH solely through light-intensity modulation. Consequently, the graphene/WSe_2 synaptic device shows tunable optical potentiation and depression behavior with an ultralow power consumption of 127 aJ. The study further unravels the complex interplay of gate bias and incident light power in determining the sign and magnitude of the photocurrent, showing the critical role of charge trapping and photogating at interfaces. Interestingly, it is found that switching between PPC to NPC can be also obtained at 0 mV drain-source voltage. Overall, the reversible potentiation/depression effect based on light intensity modulation and its combination with additional gate bias tunability is very appealing for the development of energy-efficient optical communications and neuromorphic computing.

1. Introduction

Graphene (Gr) and transition metal dichalcogenides have emerged as excellent materials for optoelectronic devices thanks to high carrier mobility[1] and strong light absorption across the visible range,[1] respectively. Because of the absence of dangling bonds on their surfaces, graphene and transition metal dichalcogenides can also be freely stacked to form van der Waals heterojunctions (vdWH), which can effectively harness photons and exhibit ultrahigh responsivity.[2] However, photoexcited carriers can get captured by local potential fluctuations on the trap sites of vdWHs, inhibiting fast recombination and limiting the device response time.[3] While extremely detrimental for photodetection applications, this mechanism opens new opportunities toward vdWHs applications in the field of neuromorphic devices, such as synaptic devices and brain-like computing chips.[4] In fact, trapped charges result in a photogating effect, i.e., a shift in the Fermi level of graphene.[5] This can be leveraged to optically modulate the sign and magnitude of the photoconductivity, in principle eliminating the need for an external gate bias and minimizing the overall energy consumption.

Current photosynapses based on vdWHs are mostly three-terminal devices, where the photoresponse is controlled through the gate bias.[6] Pradhan et al.[7] used graphene-perovskite quantum dot hybrids as the basis for optoelectronic synapses in the field of facial recognition. In the reported device photogenerated electrons accumulate in the perovskite quantum dots. This results in photogating and produces a hole current in the graphene channel. In this case, the dominant carrier type in the channel is modulated through the gate voltage. Yu et al.[8] proposed a bioinspired mechano-photonic artificial synapse which is composed of a Gr/MoS_2 heterostructures-based phototransistor and an integrated triboelectric nanogenerator, the latter modulating the optoelectronic synaptic behavior. Kim et al.[9] fabricated a MoS_2/hBN/WSe_2/Gr gate-tunable optoelectronic synapse device based on the tunneling of electrons or holes between the WSe_2 channel and the floating gate. The devices performed learning and recognition tasks by using the artificial neural network based on a single-layer perceptron model and the recognition rate. Sun et al.[10] constructed an asymmetric WSe_2/Gr heterostructure to achieve optical modulation of hysteretic behavior. The results showed that inhibitory and excitatory synapses can be switched by changing the polarity of the electrical spikes through gate bias.

H. Tang[+], T. Anwar, G. Tagliabue
Laboratory of Nanoscience for Energy Technologies (LNET)
École Polytechnique Fédérale de Lausanne
Station 9, Lausanne CH-1015, Switzerland
E-mail: giulia.tagliabue@epfl.ch

M. S. Jang
School of Electrical Engineering
Korea Advanced Institute of Science and Technology
Daejeon 34141, Republic of Korea

The ORCID identification number(s) for the author(s) of this article can be found under https://doi.org/10.1002/advs.202309876

[+]Present address: Academy of Engineering & Technology, Fudan University, Handan Road 220, Shanghai 200433, China

© 2024 The Authors. Advanced Science published by Wiley-VCH GmbH. This is an open access article under the terms of the Creative Commons Attribution License, which permits use, distribution and reproduction in any medium, provided the original work is properly cited.

DOI: 10.1002/advs.202309876

21983844, 0, Downloaded from https://onlinelibrary.wiley.com/doi/10.1002/advs.202309876, Wiley Online Library on [28/04/2024]. See the Terms and Conditions (https://onlinelibrary.wiley.com/terms-and-conditions) on Wiley Online Library for rules of use; OA articles are governed by the applicable Creative Commons License

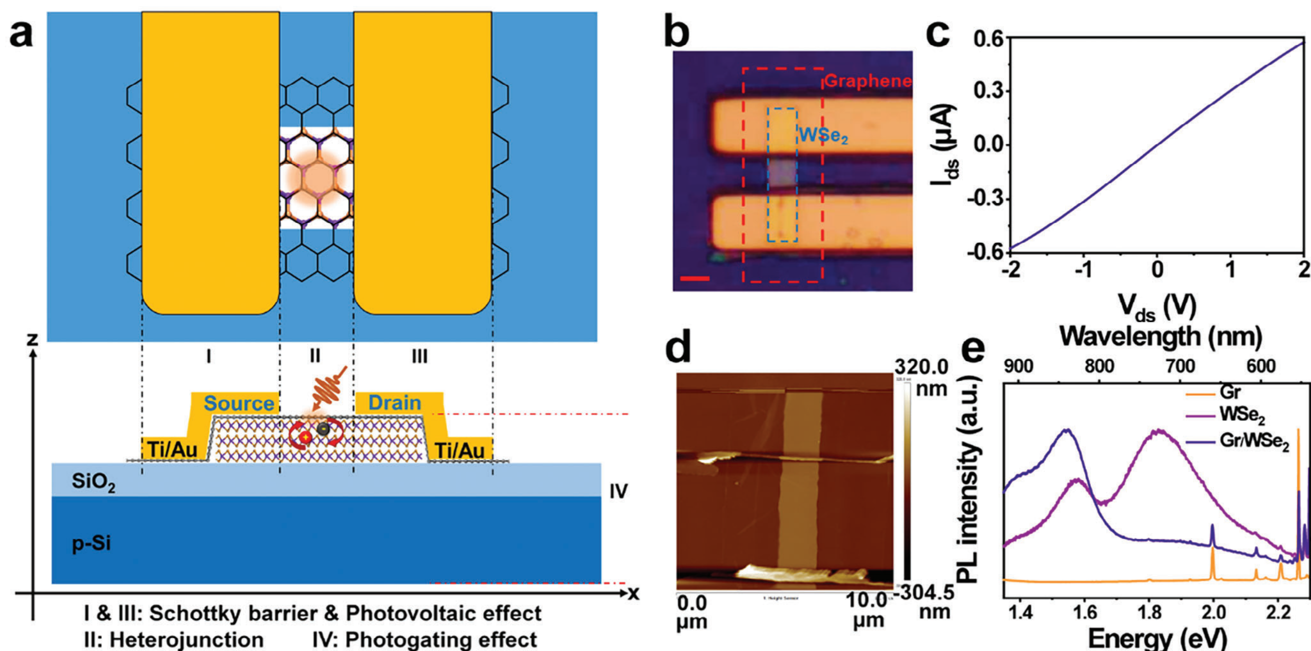

Figure 1. a) Schematic of the Gr/WSe_2 heterojunction-based device. b) Optical image of Gr/WSe_2 heterojunction-based device. The scale bar indicates 5 μm. c) Current–voltage characteristics of the device under dark. d) The AFM image of the heterojunction, and e) PL spectra of the pristine graphene (orange), the pristine WSe_2 (purple), and Gr/WSe_2 heterojunction (royal) at room temperature.

Overall, to date, the photogating effect was used to modulate the carrier concentration in the vdWH by changing the intensity of the light. Most of the cases show that the carrier concentration increases monotonously with illumination intensity, while electrical stimuli can modulate the charge transfer and determine the sign of the photocurrent. Therefore, optical stimulation is used for synaptic potentiation while electrical stimulation is required for synaptic depression.[11] However, electrical stimuli result in additional energy consumption and limit the integration of complex 2D materials-based devices, which is a significant disadvantage of optoelectronic synapses. Therefore, it is necessary to integrate optical potentiation and depression within one device, using a single optical stimulus.

In this paper, we report an optoelectronic synaptic device based on Gr/WSe_2 vdWH that exhibits tunable optical potentiation and depression performance simply by adjusting the incident light power. This is achieved thanks to charge trapping at different interfaces present in the device. The photogating mechanism is systematically analyzed considering the shift of the Dirac point, the photoconductivity flipping point, and the role of impurities density. It is found that the gate bias and laser power can modulate the photogating level as well as the sign and magnitude of the photocurrent. Besides, this optoelectrical synapse successfully carried out typical synaptic functions, including excitatory postsynaptic current (EPSC), inhibitory postsynaptic current (IPSC), and paired-pulse facilitation (PPF). In addition, the synaptic plasticity was successfully modulated by varying the parameters of light spikes. It is worth noting that it has an extremely low electrical power consumption of ≈127 aJ. This work provides a strategy to fabricate fully optical-modulated neuromorphic devices.

2. Results and Discussion

The Gr/WSe_2 three-terminal device is constructed by first dry-transferring a WSe_2 multi-layer flake onto a SiO_2/Si substrate, where Si can be used to apply a gate bias (V_{gs}). Subsequently, the WSe_2 flake is etched into a 15 μm × 5 μm rectangle. Next, monolayer graphene (Graphenea, Inc.) is wet-transferred over the WSe_2 patch and etched into a ribbon with length and width of 20 and 10 μm, respectively (see **Figure** 1a,b and Experimental Section). Finally, source (s) and drain (d) Ti/Au contacts are evaporated to contact the graphene ribbon. With this device geometry, graphene short-circuits WSe_2, and it is possible to minimize the photoresponse which is otherwise induced by the distinct Schottky barriers created at the Gr/Au and WSe_2/Au contacts. The current–voltage characteristics of the device in the dark (Figure 1c), measured as the source-drain current, I_{ds}, as a function of the source-drain voltage, V_{ds}, show a weak rectification behavior in the high voltage section (1 to 2 V), caused by the Schottky contact between graphene and Ti/Au. An atomic force microscopy (AFM) image of the Gr/WSe_2 device is shown in Figure 1d. The thickness of the WSe_2 flake is 5 nm. The surface of the device is flat and uniform. Photoluminescence spectroscopy in Figure 1e reveals that, from 1.2 to 2 eV, light emission is quenched in the heterojunction compared to pristine WSe_2. This indicates that charges in the interlayer were coupled between graphene and WSe_2 in the wavelength range of 750–620 nm.[12]

To avoid any photoinduced carriers generated in the Gr/Ti/Au junction region, we used a laser source with a 4.4 μm illumination spot diameter located at the center of the heterojunction. Overall, in this structure graphene works as the carrier transport channel and WSe_2 contributes the electron–hole pairs under

 © 2024 The Authors. Advanced Science published by Wiley-VCH GmbH

21983844, 0, Downloaded from https://onlinelibrary.wiley.com/doi/10.1002/advs.202309876, Wiley Online Library on [28/04/2024]. See the Terms and Conditions (https://onlinelibrary.wiley.com/terms-and-conditions) on Wiley Online Library for rules of use; OA articles are governed by the applicable Creative Commons License

illumination. Under illumination, several distinct effects are expected to play a role in determining the overall device photoresponse. First of all, any unavoidable asymmetry between the source/drain Gr/Ti/Au contacts[13] creates a built-in potential and therefore a source/drain photovoltage under illumination (see Region I, II, and IV in Figure 1a). Furthermore, defects and impurities in vdWHs can act as trap centers, resulting in photogating effects[14] (see Region III and IV in Figure 1a). Thus, two photogating contributions are expected in this system, originating from the Gr/WSe_2 vdWHs and WSe_2-SiO_2-Si[15] and Gr-SiO_2-Si[16] interfaces, respectively. Importantly, the relative band position of each interface in different operating conditions (gate bias and laser power) will determine the net photogating effect. Overall, it is the interplay of these different effects that determines the sign of the photocurrent and whether illumination results in potentiation or depression of the device (shown in **Figure 2**). Thus, we first characterize the device photoresponse in a broad range of operating conditions and subsequently demonstrate its operation as a synaptic device controlled solely by the laser intensity.

2.1. Optoelectronic Response of Graphene/WSe_2 Devices

The current-voltage curves of the Gr/WSe_2 device under illumination and in the dark are shown in Figure S1 (Supporting Information). Here, the photocurrent (I_{ph}) in the Gr/WSe_2 device is defined as the difference between the source-drain currents under illumination and in the dark, i.e., $I_{ph} = I_{Light} - I_{Dark}$. As shown in Figure 2a, at $V_{gs} = 0$ V and under 635 nm illumination, I_{ph} varies with increasing incident laser power (P_{in}). Interestingly, in Figure 2a, when V_{ds} is zero, I_{ph} is negative. This can be associated with the unavoidable asymmetries at the two metal/graphene contacts resulting in a small built-in electrical potential difference (≈0.2 mV, see Figure S2, Supporting Information).[17] Furthermore, under illumination, a non-zero photovoltage is generated at each metal/graphene contact,[18] which is estimated in the range of 0.4–0.6 mV (Figure S2; Section S1, Supporting Information). Overall, it is possible to define an effective drain-source voltage (V_{ds}^{eff}) under illumination as:

$$V_{ds}^{eff} = V_{ds} + V_{PV} \tag{1}$$

The sign of V_{ds}^{eff} can be positive or negative depending on the interplay of the different terms. Since the graphene channel is p-doped, the photocurrent at $V_{gs} = 0$ V can be given by

$$I_{pc} = \frac{e\mu_p p^* A V_{ds}^{eff}}{L} \tag{2}$$

where μ_p, p^*, A, and L are the hole mobility, photo-generated carriers, area, and length of the graphene channel, respectively. Therefore, its sign depends on V_{ds}^{eff} and the type of photogenerated carriers. Next, we applied a series of laser pulses with a duration of 5 s and increasing P_{in}, from 0.05 to 4 mW to the device. The pulse interval was 10 s. As shown in Figure 2b, for $V_{gs} = 0$ V, changing V_{ds} from 10 to -10 mV. Interestingly, when V_{ds} is small and positive (red curve), increasing P_{in} results in a change from positive photoconductivity (PPC) to negative photoconductivity (NPC). From further testing, we find that when $V_{ds} \leq -0.029$ mV, only NPC is obtained (Figure S3, Supporting Information), which means $V_{ds}^{eff} < 0$ V. Notably, when a very small V_{ds} is applied, the response time of the device slows down and a synaptic behavior occurs, which we will discuss in Section 2.2. Furthermore, as shown in Figure S4 (Supporting Information), the second pulse does not affect the first one when there is a time gap, longer than 3 s between consecutive illumination.

In addition to the effects of photovoltage and built-in electrical potential difference within the source/drain channel, the photogating effect originating from the Gr/WSe_2 vdWHs and Gr-WSe_2-SiO_2-Si interfaces affects the photoresponse in this system. In particular, it is known that in heterojunctions with low dimensional materials, defects and impurities in the structure can work as trap centers.[14] If one type of photogenerated carrier is trapped for a time τ, which is greater than $\tau = L^2/\mu V_{ds}$, the average time for the carriers to move through the graphene channel,[14] carrier accumulation will occur at the interface providing an additional gate voltage, ΔV_G. To assess the role of photogating, we applied different gate biases (V_{gs}) to the device and measured the transfer curves of the device for different P_{in} (Figure 2c). As the P_{in} increases, the Dirac point shifts to higher V_{gs}, suggesting a negative gating ($\Delta V_G < 0$) caused by trapped electrons in trap centers. Here, the photocurrent generated by the photogating effect can be expressed as[14]

$$I_{pg} = g_m \Delta V_G \tag{3}$$

where g_m is the transconductance. ΔV_G is the horizontal displacement of the transfer characteristic curve. As shown in Figure 2d, the device shows gate-tunable positive and negative photoresponse. When $V_{gs} < V_{Dirac_dark}$, the majority carrier in dark is the holes ($g_m < 0$), thus according to Equation (3), it shows PPC ($I_{ph} > 0$). While at $V_{gs} > V_{Dirac_dark}$, the majority carrier in dark is electron ($g_m > 0$), NPC occurs ($I_{ph} < 0$). However, there exists a regime where both g_m and I_{ph} are negative due to photoconductive components as shown in **Figure 3**. Furthermore, the peak photocurrent is associated with the V_{Dirac}, because the device reaches a high electrostatic doping with either electrons or holes.[19]

The dynamic current responses of the device for different gate biases under various laser power illuminations are shown in Figure 2e. For $V_{gs} < 0$ V, the device initially exhibits PPC. As P_{in} increases, the photoconductivity flips to negative. It is important to note that the photodoping effect is not sufficient to explain the switchable photocurrent of this device. As shown in Figure S5 (Supporting Information), it is found that the I_{ds}-V_{gs} shift under illumination is induced by both photogating and photoconductive effects. Indeed, I_{ds}-V_{gs} not only shifts to the right but also moves down. The ΔV_G shifts to higher V_{gs} corresponds to graphene becoming deeply p-doped, with a down-shift of its E_F. Normally, this entails a photocurrent increase as many holes move into graphene. However, in our case, the photocurrent decreases with increasing P_{in}, which is then most likely related to the n-doping effect from impurities.

We further note that the dark current/gate-bias curve after each illumination cycle is shifted left and downwards compared to the previous dark transfer curve (see dash lines in Figure 2c and blue line in Figure S5, Supporting Information). It reveals that the trapped carriers are not immediately released when the

© 2024 The Authors. Advanced Science published by Wiley-VCH GmbH

21983844, 0, Downloaded from https://onlinelibrary.wiley.com/doi/10.1002/advs.202309876, Wiley Online Library on [28/04/2024]. See the Terms and Conditions (https://onlinelibrary.wiley.com/terms-and-conditions) on Wiley Online Library for rules of use; OA articles are governed by the applicable Creative Commons License

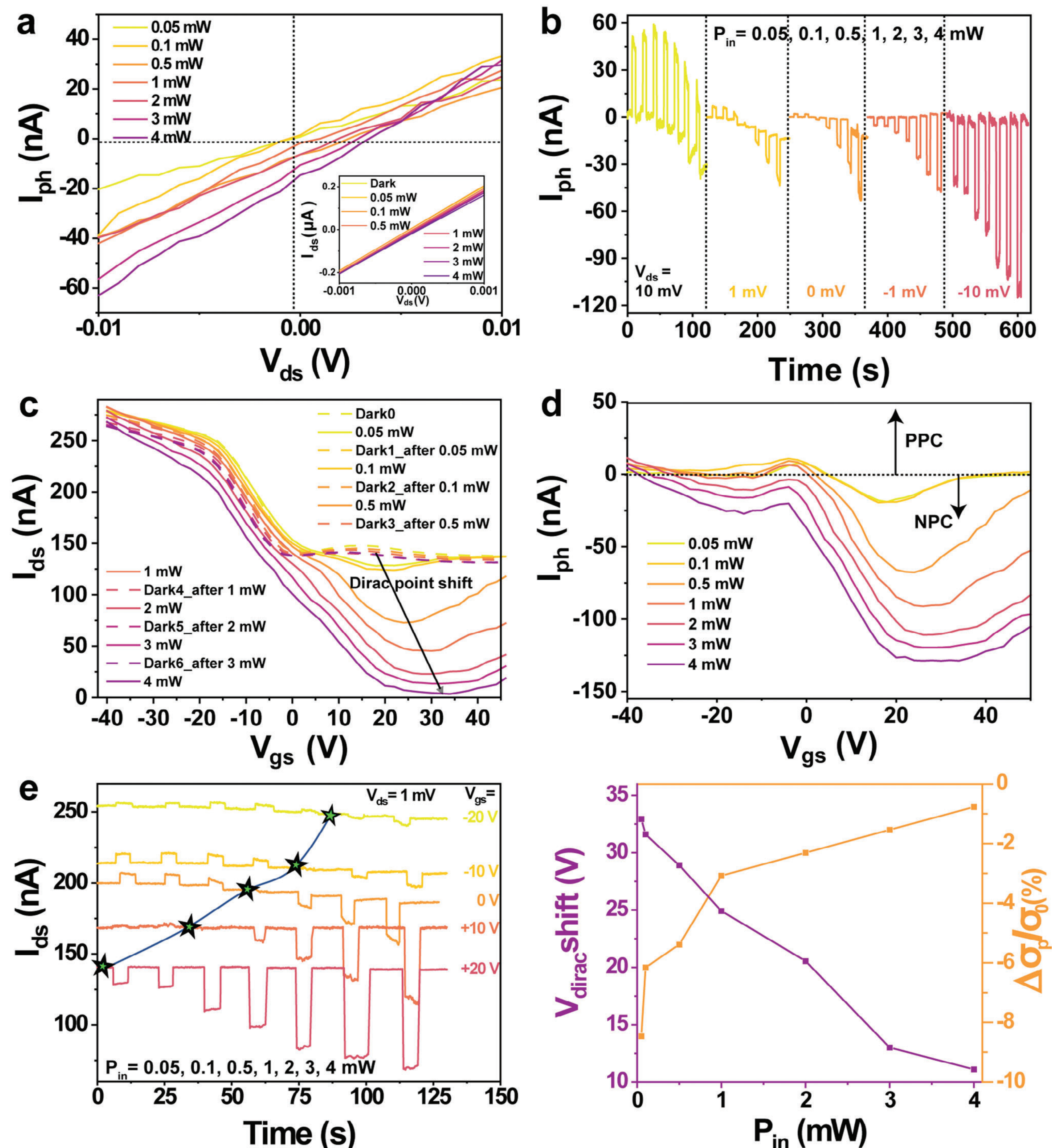

Figure 2. a) The photocurrent (I_{ph}) of the Gr/WSe$_2$ heterojunction-based device under illumination (635 nm, 0.05-4 mW) at $V_{gs} = 0$. The inset enlarged image shows the output curve from −0.1 to 0.1 mV. b) Dynamic photocurrent current change at $V_{gs} = 0$ V and different P_{in} for a series of V_{ds}. c) Transfer characteristics of the Gr/WSe$_2$ device at different illumination powers (solid lines) and in the dark after each illumination condition (dash lines). It shows the shift of the Dirac point for a constant $V_{ds} = 1$ mV. d) The photocurrent of the Gr/WSe$_2$ device at different illumination power. e) Dynamic current change at different P_{in} after applying different V_{gs} for a constant $V_{ds} = 1$ mV. f) Shift of Dirac point and the fractional change in dark conductivity (at zero gate bias) after different P_{in}.

 © 2024 The Authors. Advanced Science published by Wiley-VCH GmbH

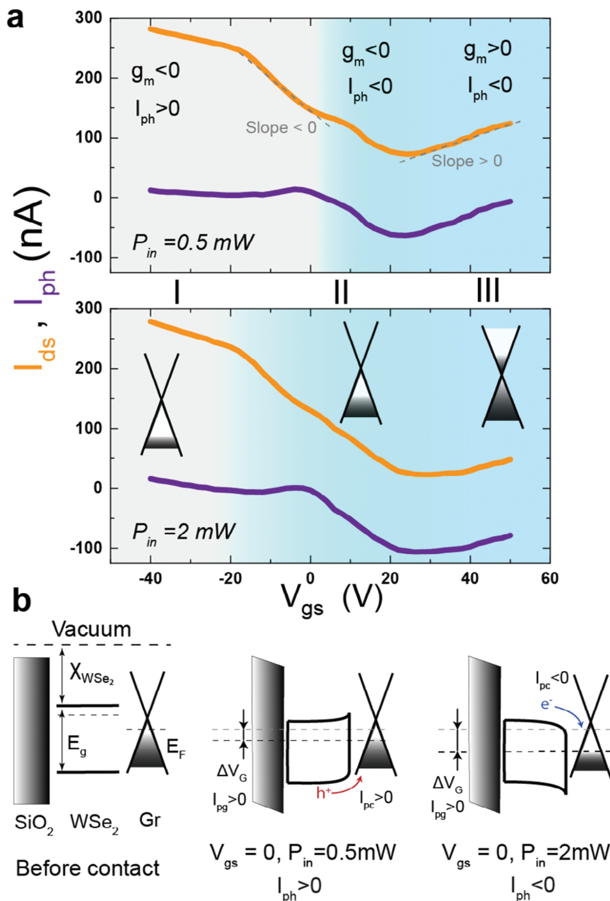

Figure 3. Mechanism for flipping in the sign of the photocurrent in Gr/WSe_2 heterojunction by changing V_{gs} and P_{in}. a) Drain source current and photocurrent (I_{ph})with varying V_{gs} and different applied P_{in}, 0.5 mW (top panel) and 2 mW (bottom panel). Three different regions have been identified depending on the sign of transconductance (g_m) and net I_{ph}. PPC is observed in region I, while regions II and III show NPC. The photogenerated carriers injected from WSe_2 give rise to the photoconductive component of the resultant photocurrent. At high power this becomes more negative and grows in magnitude, thus broadening the region II. b) Band diagram for three different conditions: (left panel) before contact, X_{WSe2} is the WSe_2 electron affinity, E_g is the WSe_2 bandgap, E_F is the fermi level of graphene; (middle panel) band alignment for $V_{GS} = 0$ and P_{in} = 0.5 mW (region I): $I_{pg} > 0$ while the upward band-bending at the WSe_2/Gr interface results in $I_{pc} > 0$ (hole injection), overall leading to $I_{ph} > 0$ (PPC); (right panel) band alignment for $V_{GS} = 0$ and $P_{in} = 2$ mW (region II): $I_{pg} > 0$ while the downward band-bending at the WSe_2/Gr interface, caused by the larger photovoltage, results in $I_{pc} < 0$ (electron injection), overall leading to $I_{ph} < 0$ (NPC). I_{pg} and I_{pc} are the photogating and photoconductive components of the photocurrent.

light is turned off. This can be related to changes in the impurity density (n_{imp}) within the substrate.[20] This effect is very pronounced in our device because of the very low initial doping of graphene and thus comparable to changes in n_{imp}, as shown by the close to zero Dirac point (dashed lines in Figure 2c). Indeed, we modeled the effect of an increase in n_{imp} on the transfer curve in the dark (Figure S6 and Section S4, Supporting Information), retrieving qualitatively the experimental trend. As the impurity density directly affects the carrier mobility in graphene,[21] ($\mu \propto 1/n_{imp}$) and in turn the dark conductivity (σ_d), we can use the experimental I_{ds}–V_{ds} dark curves (Figure S1, Supporting Information), to estimate the fractional change in σ_d after each illumination as $\frac{\Delta\sigma_d}{\sigma_0} = \frac{I_{Dark(i)} - I_{Dark0}}{I_{Dark0}}$. From Figure 2f (orange curve), we find that the conductivity in the dark decreases with increasing P_{in}. This also affects the photoconductive component of the resulting photocurrent as, $I_{pc} \propto (\Delta\sigma_d + \Delta\sigma)$, where, $\Delta\sigma$ is the photoinduced change in conductivity. For V_{ds} = 1mv, the sign of V_{ds}^{eff} does not change so, Equation (2) can be equivalently written as $\frac{I_{pc}}{I_{Dark0}} \approx \frac{\Delta\sigma_d}{\sigma_0} \pm \frac{\Delta p}{p_0}$, where Δp is the photogenerated carriers injected into the graphene channel. Thus for the case, where $\Delta\sigma_d \approx 0$, a positive (negative) photocurrent is observed if the carriers injected into the channel are the same (opposite) to the majority carrier in the channel.[14]

We note that at high power this would grow in magnitude due to an increase in photogenerated carriers in WSe_2 that can be injected into graphene. We also observed that the effect exhibits a long recovery time, which can be important for neuromorphic applications of the device discussed in Section 2.2. In addition, we interestingly observe that when the P_{in} reaches 1 mW, the Dirac point shift slows down, implying that the photogating effects become saturated (Figure 2f, purple curve). This is a typical behavior related to the gradual filling of trap states with increasing laser power.[22]

To better understand the tunable photoconductance of the device, we have identified three different regimes (I: $I_{ph} > 0$, $g_m < 0$; II: $I_{ph} < 0$, $g_m < 0$; III: $I_{ph} < 0$, $g_m > 0$) in the transfer curve under different illumination conditions as shown in **Figure 3a**. Based on the shift of the transfer curve under illumination, as discussed above, we know that trapped charges induce a negative photovoltage ($\Delta V_G < 0$), i.e., increased p-doping of graphene. Hence the sign of the photogating component of the current will depend on the transconductance of the transfer curve, specifically $I_{pg} > 0$ if $g_m < 0$ and vice versa. Looking at the orange curves in Figure 3a, we can thus conclude that $I_{pg} > 0$ for regimes I and II. On the other hand, the sign of the photoconductive current, I_{pc}, will be positive (negative) if majority (minority) carriers are injected. In regions I and II of Figure 3, graphene is p-doped. Therefore, $I_{pc} > 0$ if holes are injected and $I_{pc} < 0$ if electrons are injected. To determine which condition is occurring, we observe that in region II of Figure 3, the total sign of the photocurrent is negative. As in this regime, the photogating component is positive; the photoconductive term must be negative, meaning that electrons are injected into the p-doped graphene. Finally, from Figure 3a we note that region II broadens when going from weaker (P_{in} = 0.5 mW) to stronger (P_{in} = 2 mW) illumination intensities. Importantly, for a certain range of V_{gs}, including $V_{gs} = 0$, the sign of I_{ph} flips as the intensity of illumination increases. Overall, considering $V_{gs} = 0$ as our reference case, we can draw the band alignment depicted in Figure 3b. Under weak illumination (middle panel), the upward band-bending at the Gr/WeS_2 interface allows injection of holes in the p-doped graphene, giving a positive I_{pc} that together with a positive I_{pg} results in PPC, i.e., $I_{ph} > 0$. However, as the intensity of illumination is increased, the larger photovoltage causes a flipping of the band-bending. Hence, photogenerated electrons in WSe_2 preferentially transfer to graphene, giving a negative I_{pc} that overcomes the positive I_{pg} to produce NPC, i.e., $I_{ph} < 0$.

 © 2024 The Authors. Advanced Science published by Wiley-VCH GmbH

21983844, 0, Downloaded from https://onlinelibrary.wiley.com/doi/10.1002/advs.202309876, Wiley Online Library on [28/04/2024]. See the Terms and Conditions (https://onlinelibrary.wiley.com/terms-and-conditions) on Wiley Online Library for rules of use; OA articles are governed by the applicable Creative Commons License

21983844, 0, Downloaded from https://onlinelibrary.wiley.com/doi/10.1002/advs.202309876, Wiley Online Library on [28/04/2024]. See the Terms and Conditions (https://onlinelibrary.wiley.com/terms-and-conditions) on Wiley Online Library for rules of use; OA articles are governed by the applicable Creative Commons License

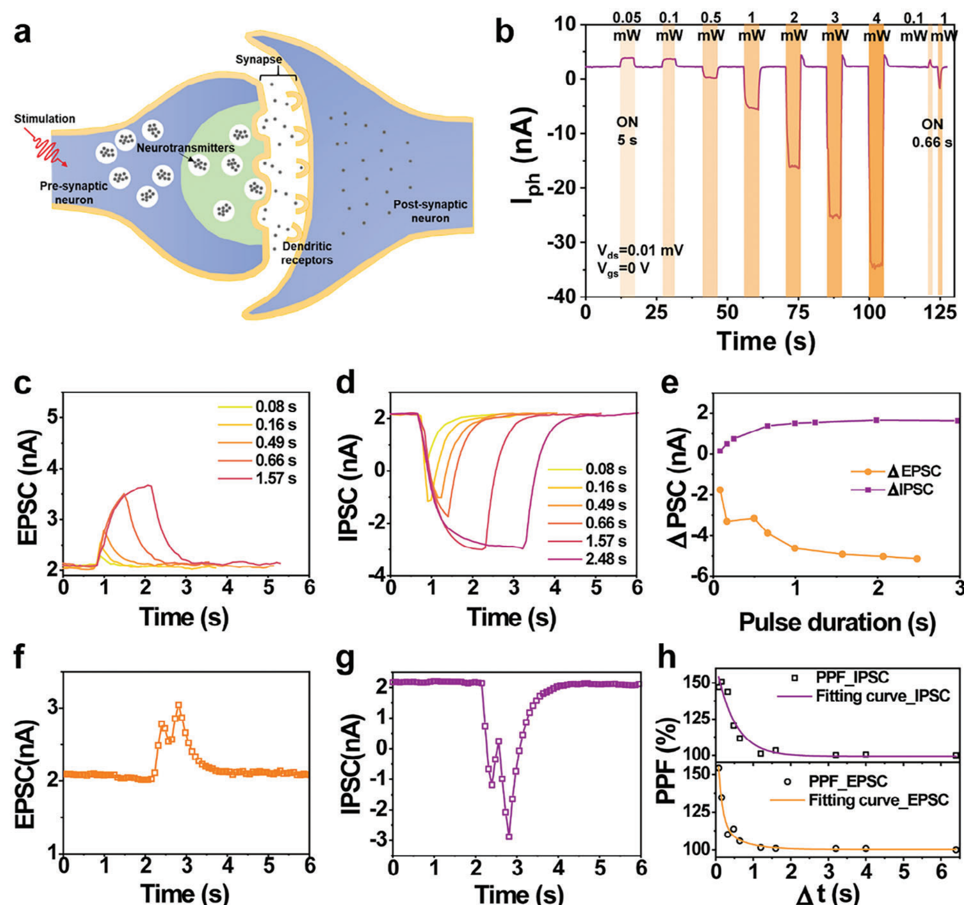

Figure 4. a) Schematic Diagram of signal transmission in biological synapses b) Dynamic change of I_{ds} after illumination with different laser power at different laser pulse duration, $V_{gs} = 0$ V, $V_{ds} = 0.01$ mV. c) EPSC induced by the light spike of fixed light intensity (635 nm, 0.1 mW) with different spike duration; d) IPSC induced by the light spike of fixed light intensity (635 nm, 1 mW) with different pulse duration; e) change of EPSC and IPSC with different pulse duration. f) EPSC induced by two consecutive light spikes (635 nm, 0.1 mW, 1 s) with a spike interval of 1 s; g) IPSC induced by two consecutive light spikes (635 nm, 1 mW, 1 s) with a spike interval of 1 s; h) PPF of ratio versus interstimulus time for EPSC and IPSC; $V_{ds} = 0.01$ mV and $V_{gs} = 0$ V.

2.2. Neuromorphic Optoelectronic Synapse

The transmission of information in the human brain depends on synapses. **Figure 4a** is a schematic diagram of signal transmission in an organism through synapses between neurons. After receiving the external stimulus, neurotransmitters will be released from the anterior neuron to the posterior neuron in the form of exocytosis, causing changes in electrical signals. In biological postsynaptic neurons, the synaptic potentials lead to excitatory postsynaptic current (EPSC) or inhibitory postsynaptic current (IPSC), which respectively determine the gain or loss of synaptic weight. The dynamic photoresponse of our device was tested to assess its synaptic behavior. As mentioned in Section 2.1, the device response at $V_{ds} = 0.01$ mV was similar to that at higher V_{ds}. To avoid the influence on I_{ds} from gate bias, we set $V_{gs} = 0$ V and operate the device using light as the only input energy. From Figure 4b and Figure S7 (Supporting Information), we found that when the laser pulse duration is 5 s, the device took ≈1–2 s to stabilize. Unlike the recently reported photonic synapses, we can switch between EPSC and IPSC for the Gr/WSe_2 device by changing solely the incident laser power (P_{in}). When stimulating the Gr/WSe_2 device at 635 nm with a P_{in} less than 0.5 mW, we observed EPSC; when the P_{in} is >0.5 and <3 mW, we instead obtained IPSC. Also, we carried out a dynamic photoresponse test for the device at $P_{in} = 0.1$ and 1 mW with 0.66 s laser pulse duration and observed a typical EPSC and IPSC performance.

Synaptic plasticity is the basic function of the human brain to carry out advanced learning instructions, which can be divided into short-term plasticity and long-term plasticity. Short-term plasticity has a retention time of several hundred milliseconds to a few minutes and plays an important role in the processing or learning of temporary information. As shown in Figure 4c,d, we applied fixed incident light power of 0.1 and 1 mW, respectively with different pulse durations.

Paired pulse facilitation (PPF) is a typical form of short-term plasticity. After 2s of illumination at 635 nm wavelength with a P_{in} of 0.1 mW, a single EPSC behavior appeared. After 1 s interval, the light pulse under the same conditions was applied again. The secondary current increase value (A_2) was higher than the primary current increase value A_1, indicating that the Gr/WSe_2

 © 2024 The Authors. Advanced Science published by Wiley-VCH GmbH

21983844, 0, Downloaded from https://onlinelibrary.wiley.com/doi/10.1002/advs.202309876, Wiley Online Library on [28/04/2024]. See the Terms and Conditions (https://onlinelibrary.wiley.com/terms-and-conditions) on Wiley Online Library for rules of use; OA articles are governed by the applicable Creative Commons License

Table 1. Comparison of energy consumption of various optoelectrical synaptic devices.

Devices	λ [nm]	EPSC/IPSC [nA]	1st PPF ratio	Modulation of potentiation and depression	Power consumption	Ref.
Gr/WSe_2	635	6	1.5 @Δt = 80 ms	single wavelength light-potentiation and depression	127 aJ	This work
TIPS-pentacene/PS OTFT	450	3.39	1.7 @Δt = 50 ms	light-potentiation /electric-depression	36 aJ	[24]
Black phosphorus /CdS	450	1250	/	light-potentiation /electric-depression	4780 aJ	[25]
POx/black phosphorus	280,365	≈100	≈0.3 @Δt = 100 ms	285 nm light-potentiation/365 nm light-depression	3.5e6 aJ	[26]
Ag-TiO_2	350–650	≈300	≈1.8 @Δt = 10 µs	Visible light-potentiation/UV light-depression	≈2.4e10 aJ	[27]

vdWH device still retained the primary light stimulation behavior when the second light stimulation was performed (Figure 4e). The biomimetic synaptic behavior of the device can be further characterized by the PPF index, defined as:

$$\mathrm{PPF} = \frac{A_2}{A_1} \times 100\% \tag{4}$$

where A_1 is the EPSC amplitude of the first light pulse stimulation, and A_2 is the EPSC amplitude of the second light pulse stimulation under the same conditions. The PPF values were calculated according to Equation (1) by changing the interval time (Δt) between two successive light pulses from 80 to 160 ms, 490 ms, 660 ms, 1570 ms, and 2480 ms. As can be seen from Figure 4f,g, PPF decreases gradually with the increase of Δt. It is found that the downward trend of PPF can be fitted with a double exponential function (Equation (5))

$$\mathrm{PPF} = C_1 \exp\left(-\frac{\Delta t}{\tau_1}\right) + C_2 \exp\left(-\frac{\Delta t}{\tau_2}\right) + 1 \tag{5}$$

where C_1 and C_2 represent the fast and slow speed promotion amplitude, while τ_1 and τ_2 represent the fast and slow speed characteristic relaxation time, respectively. The red line in Figure 4h is the double exponential function curve fitted according to Equation (2). For EPSC we found that $\tau_1 = 0.11$ s and $\tau_2 = 0.56$ s, while for IPSC we obtained 0.49 and 0.49 s respectively, similar to the time scale of biological synapses.[23]

The potential applications of artificial synapses in neuromorphic circuits limit their energy consumption. Although several remarkable devices and materials simulating synaptic function (electrical or optical) have recently been reported (listed in **Table** 1), the energy consumption is still several orders of magnitude higher than that of biological synapses (≈10 fJ per activity). Our Gr/WSe_2 optoelectric synapse's average energy consumption (E_{ave}) during training can be calculated from the training voltage (V), the delta value of conductance before and after training (ΔG), the duration of the light spike (t), and the number of spikes (N). Thus, $E_{ave} = (V^2 \times \Delta G \times t)/N = (V \times \Delta I_{dark} \times t)/N$, where $\Delta I_{dark} = 0.159$ nA, $t = 80$ ms, V = 0.01 mV, N = 1. It results in >0.4% conductivity change (high enough to simulate all synaptic functions) with an average active area of 15.2 µm^2 with an illuminating power of 0.1 mW and duration of 80 ms µm^{-2}, consuming $E_{ave} \approx 127$ aJ for each synaptic activity. The results indicate that the photogating effect contributes to the synaptic behavior, and the photovoltaic effect is used to convert the energy of the photons to electrical energy and make the power consumption of the device ultralow.

3. Conclusion and Perspective

In summary, we demonstrated a photogating mechanism for Gr/WSe_2 vdWH optoelectronic synaptic devices that offers switching between NPC and PPC with ultralow electrical power consumption, relying solely on the intensity of the optical stimuli. Through careful characterization, we elucidated the complex interplay of photovoltage and photogating at the different interfaces. We first showed that the switching behavior depends on the sign of the effective drain-source voltage V_{ds}^{eff} and requires only small V_{ds} to occur. Second, the contribution of photogating across the multiple interfaces of the Gr/WSe_2/SiO_2/Si structure was deconvoluted. The results show that gate bias and laser power can modulate the sign and magnitude of photocurrent because the photogating effects in the trap centers induce different levels of band bending in each interface. Notably, when a very small V_{ds} is applied, the response time of the device slows down and presents a synaptic behavior. Consequently, we confirmed and quantified typical synaptic functions, including EPSC, IPSC, and PPF. Moreover, the synaptic plasticity was successfully modulated by varying the parameters of light spikes. It is worth noting that it has an extremely low electrical power consumption of ≈127 aJ because of the photovoltaic effect induced by the Schottky contact between Gr and metal. Overall, this work provides a strategy to achieve all-optical modulation of neuromorphic devices with a single monochromatic light source. It could therefore advance the development of integrated neuromorphic computing systems.

4. Experimental Section

Device Fabrication: WSe_2 flakes (2D Semiconductors Int.) were mechanically exfoliated and then transferred to 300 nm SiO_2/Si substrates, where Si can be used to apply a gate bias (V_{gs}). Subsequently, the WSe_2 multi-layer flake was etched into a 15 um×5um rectangle through photolithograph and XF_4 gas etching. Monolayer graphene was ordered from Graphenea Int., and a typical polymethyl methacrylate-assisted wet transfer method was used to stack graphene over the WSe_2. After wet transferring, the monolayer graphene was etched into a ribbon with length

© 2024 The Authors. Advanced Science published by Wiley-VCH GmbH

and width of 20 and 10 µm through photolithograph and O_2 plasma dry-etching. Finally, laser writing (MLA150, Heidelberg Instruments Int.) and e-beam evaporation (LAB 600H, Leybold Optics) were used to define contacts to the heterostructures, where source (s) and drain (d) Ti/Au (5/50 nm) contacts are evaporated to contact the graphene ribbon. (see Figure S8; Section S5, Supporting Information).

Device Characterization: The Raman and photoluminescence (PL) spectra were obtained via Raman Microscope (Renishaw Ltd. Co., inVia) using an excitation wavelength of 532 nm. The flake thickness and topography were tested by AFM (Bruker, FastScan). The photoelectrical characterization is done by using a home-built set-up (see Figure S9 and Section S6, Supporting Information), which consists of a black sealed box, several optical paths, a motorized probe station (miBot, Imina Technologies), a camera, and two Keithely 2450 source meters. The source meters were used for applying source-drain bias (V_{ds}) and source-gate bias (V_{gs}). To reduce the thermoelectric effect induced by electrical tests, the delay of sweeping V_{ds} and V_{gs} was set as 1 ms. Because the samples are very sensitive to ambient moisture, we stored them in the N_2 gas tank before and after photoelectrical tests. During tests, dry N_2 with a low flow rate was injected into the black sealed box to keep it dry.

Supporting Information

Supporting Information is available from the Wiley Online Library or from the author.

Acknowledgements

This was supported by the Swiss National Science Foundation (SNSF) through the Korean-Swiss Science and Technology Cooperation Fund (Grant No. IZKSZ2_188341). M.S.J. acknowledges the support by the National Research Foundation of Korea (NRF) funded by the Ministry of Science and ICT (grants Nos. 2019K1A3A1A14064929 and 2022R1A2C2092095). The authors also acknowledge the support of the following experimental facilities at EPFL: Center of MicroNanoTechnology (CMi). The authors also acknowledge the contribution of Dr. Junbo He to the graphic abstract.

Conflict of Interest

The authors declare no conflict of interest.

Data Availability Statement

The data that support the findings of this study are available from the corresponding author upon reasonable request.

Keywords

graphene/WSe_2 van der Waals heterojunction, optoelectronic synapses, photogating, phototransistors

Received: December 16, 2023
Revised: March 28, 2024
Published online:

[1] Q. X. Qiu, Z. M. Huang, *Adv. Mater.* **2021**, *33*, 2008126.
[2] S. J. Liang, B. Cheng, X. Y. Cui, F. Miao, *Adv. Mater.* **2020**, *32*, 1903800.
[3] Y. Wang, L. Yin, W. Huang, Y. Y. Li, S. J. Huang, Y. Y. Zhu, D. R. Yang, X. D. Pi, *Adv Intell. Syst.-Ger* **2021**, *3*, 2000099.
[4] P. V. Pham, S. C. Bodepudi, K. Shehzad, Y. Liu, Y. Xu, B. Yu, X. F. Duan, *Chem. Rev.* **2022**, *122*, 6514.
[5] S. Kim, S. G. Menabde, M. S. Jang, *Adv. Electron. Mater.* **2019**, *5*, 1800940.
[6] a) K. C. Kwon, J. H. Baek, K. Hong, S. Y. Kim, H. W. Jang, *Nano-Micro Lett.* **2022**, *14*, 71. b) S. J. Liang, Y. X. Li, B. Cheng, F. Miao, *Small Struct.* **2022**, *3*, 2200064. c) Z. E. Xia, J. R. Wang, Z. E. Fei, *Phys Status Solidi-R* **2019**, *13*, 1900082.
[7] B. Pradhan, S. Das, J. X. Li, F. Chowdhury, J. Cherusseri, D. Pandey, D. Dev, A. Krishnaprasad, E. Barrios, A. Towers, A. Gesquiere, L. Tetard, T. Roy, J. Thomas, *Sci. Adv.* **2020**, *6*, eaay5225.
[8] J. R. Yu, X. X. Yang, G. Y. Gao, Y. Xiong, Y. F. Wang, J. Han, Y. H. Chen, H. Zhang, Q. J. Sun, Z. L. Wang, *Sci. Adv.* **2021**, *7*, eabd9117.
[9] S. H. Kim, M. U. Park, C. Lee, S. G. Yi, M. Kim, Y. Choi, J. H. Cho, K. H. Yoo, *Nanoscale Adv.* **2021**, *3*, 4952.
[10] Y. L. Sun, Y. X. Lin, A. Zubair, D. Xie, T. Palacios, *2D Mater.* **2021**, *8*, 035034.
[11] X. W. Feng, X. K. Liu, K. W. Ang, *Nanophotonics-Berlin* **2020**, *9*, 1579.
[12] X. Xing, L. T. Zhao, W. J. Zhang, Z. Wang, H. M. Su, H. Y. Chen, G. H. Ma, J. F. Dai, W. J. Zhang, *Nanoscale* **2020**, *12*, 2498.
[13] Y. Q. Wu, D. B. Farmer, F. N. Xia, P. Avouris, *Proc. IEEE* **2013**, *101*, 1620.
[14] H. Fang, W. Hu, *Adv. Sci.* **2017**, *4*, 1700323.
[15] M. M. Furchi, D. K. Polyushkin, A. Pospischil, T. Mueller, *Nano Lett.* **2014**, *14*, 6165.
[16] F. Luo, M. J. Zhu, Y. Tan, H. H. Sun, W. Luo, G. Peng, Z. H. Zhu, X. A. Zhang, S. Q. Qin, *AIP Adv.* **2018**, *8*, 115106.
[17] K. Nagashio, A. Toriumi, *Jpn. J. Appl. Phys.* **2011**, *50*, 070108.
[18] J. J. Chen, Q. S. Wang, J. Meng, X. X. Ke, G. Van Tendeloo, Y. Q. Bie, J. K. Liu, K. H. Liu, Z. M. Liao, D. Sun, D. P. Yu, *ACS Nano* **2015**, *9*, 8851.
[19] M. Freitag, T. Low, F. N. Xia, P. Avouris, *Nat. Photonics* **2013**, *7*, 53.
[20] Y. M. Shi, X. C. Dong, H. Tantang, C. H. Weng, F. M. Chen, C. W. Lee, K. K. Zhang, Y. Chen, J. L. Wang, L. J. Li, *J. Phys. Chem. C* **2008**, *112*, 18201.
[21] T. Fang, A. Konar, H. Xing, D. Jena, *Phys. Rev. B* **2008**, *78*, 205403.
[22] P. C. Y. Chow, N. Matsuhisa, P. Zalar, M. Koizumi, T. Yokota, T. Someya, *Nat. Commun.* **2018**, *9*, 4546.
[23] F. Q. Zhang, C. Y. Li, Z. Y. Li, L. X. Dong, J. Zhao, *Microsyst. Nanoeng.* **2023**, *9*, 16.
[24] Z. H. Shen, Z. X. Yang, Y. Q. Zhou, Y. L. Ye, B. Q. Ye, Q. C. Huang, W. B. Wu, H. Y. Hong, Z. Q. Hong, Z. Y. Meng, Z. W. Zeng, S. W. Ye, Z. M. Cheng, Q. T. Lan, J. X. Wang, Y. Chen, H. Zhang, T. L. Guo, Y. Ye, Z. Z. Weng, Y. Y. Chen, *J. Mater. Chem. C* **2023**, *11*, 3213.
[25] G. Q. Li, *Light-Sci Appl* **2023**, *12*, 24.
[26] T. Ahmed, S. Kuriakose, E. L. H. Mayes, R. Ramanathan, V. Bansal, M. Bhaskaran, S. Sriram, S. Walia, *Small* **2019**, *15*, 1900966.
[27] X. Y. Shan, C. Y. Zhao, X. N. Wang, Z. Q. Wang, S. C. Fu, Y. Lin, T. Zeng, X. N. Zhao, H. Y. Xu, X. T. Zhang, Y. C. Liu, *Adv. Sci.* **2022**, *9*, 2104632.

 © 2024 The Authors. Advanced Science published by Wiley-VCH GmbH

21983844, 0, Downloaded from https://onlinelibrary.wiley.com/doi/10.1002/advs.202309876, Wiley Online Library on [28/04/2024]. See the Terms and Conditions (https://onlinelibrary.wiley.com/terms-and-conditions) on Wiley Online Library for rules of use; OA articles are governed by the applicable Creative Commons License